

Thermal decomposition of 1-ethyl-3-methylimidazolium acetate

Dzmitry Zaitsau^a, Maxim Papusha^b, Wassja A. Kopp^b and Kai Leonhard^{b,1}

To be submitted to J Mol Liq

^aInstitute of Technical Thermodynamics, University of Rostock, Albert-Einstein-Str. 2, 18059 Rostock, Germany

^bInstitute of Technical Thermodynamics, RWTH Aachen University, Schinkelstr. 8, 52062 Aachen, Germany

Abstract

To realize the potential applications of ionic liquids as working fluids and solvents one should have knowledge about their long-term stability, which depends on their thermally initiated decomposition. However, the possible decomposition pathways are not yet known accurately. 1-Ethyl-3-methylimidazolium acetate ([C₂Mim][OAc]) is widely studied and shows potential in cellulose dissolution. In this study, we investigate possible [C₂Mim][OAc] decomposition pathways by combining decomposition experiments and ab initio rate constant computations. Both approaches yield activation energies around 135 kJ·mol⁻¹, which significantly deviate from earlier TGA measurements with open surface yielding 100 - 110 kJ·mol⁻¹ and are probably affected by evaporation. Our study uses an improved TGA measurement protocol with a sealed pan with a tiny hole that fosters measurement of the actual chemical process leading to mass loss. Ab initio computations of this study comprise vapor-liquid equilibria of reactants and products as well as forward and reverse reaction rate constants in the gas and liquid phase. Calculations for the gas phase closely match a first-order analysis of the experiments, but calculations for the liquid phase strongly depend on the quality of solvation modeling. The computations indicate that the S_N2 pathway with an activation energy of 140 kJ·mol⁻¹ dominates thermal decomposition of [C₂Mim][OAc].

1. Introduction

After having been proposed as prospective solvents for chemical engineering and electrochemistry more than two decades ago, ionic liquids (ILs) have motivated a large number of scientific studies that have enabled numerous industrial applications. Thus, ILs are potential candidates for solving the technological issues in countering environment pollution as a clean, efficient, and eco-friendly alternative to volatile organic solvents. Furthermore, the properties of ILs could be tailored depending on their application by altering the combination of cations and anions. Numerous reviews[1–7] detail their physical, chemical, and transport properties relevant to industrial applications. The main trends of chemical engineering in the field of IL applications include enzymatic synthesis in ILs [8], Supported Ionic Liquid Membranes (SLM) [9], extractor agents and reaction media [10], Supported Ionic Liquid Phase (SILP) in catalysis [11–15], gas purification [16], electrodeposition from ILs [17], ILs as stationary phases for Gas and Liquid Chromatography, producing natural fibers and biomass deconstruction [18–20]. Even the list of such reviews can take a few pages. But the high expectations on the future of ILs are spoiled with two main drawbacks – high

¹ To whom correspondence should be addressed: kai.leonhard@itt.rwth-aachen.de

price and limited thermal stability, i.e. maximum operating temperatures of 470 to 570 K [21]. A higher thermal stability reduces the cost of replacing and purifying the solvent, consequently, partly resolving the issues with high prices associated with ILs. Therefore, we focus on the stability problem in this study.

Thermal decomposition significantly limits the industrial application of ILs. Decomposition products can easily spoil and deactivate catalysts; in some cases, the application of ILs containing heteroatoms like halogens, sulfur, phosphorous can lead to issues in utilization and recycling.

On the other hand, the reversible degradation can be utilized to recycle ILs. Recently, we have conducted a comprehensive thermodynamic study of 1,5-diazabicyclo[4.3.0]non-5-enium acetate ([DBNH][OAc]) [22]. This distillable IL is used in the IONCELL-F process of cellulose dissolution [23]. The distillation process of [DBNH][OAc] corresponds to reversible dissociation of IL into acetic acid and 1,5-diazabicyclo[4.3.0]non-5-ene. Thus, decomposition is not only a drawback of industrial application of ILs but can be used for purification of ILs as well.

Clearly, ILs containing only C, H, N and O exclude a wide range of harmful decomposition products mentioned above. They therefore lead to less pollution in the case of decomposition as compared to compounds (ILs) containing other elements (S, P, F, Cl, Br). For example, 1-ethyl-3-methylimidazolium acetate ([C₂Mim][OAc], CAS Nr: 143314-17-4) has shown high ecotoxicological response EC₅₀ values in biodegradability test [24], which is an evidence of its environmentally friendly behavior. The application of this IL for cellulose and biomass dissolution was studied by Sun *et al.* [25], Singh *et al.* [26], Hermanutz *et al.* [27], Kosan *et al.* [28], Zhao *et al.* [29] and other scientific groups. Thermochemical properties were already studied by Zhang *et al.* [30].

Decomposition behavior is widely studied using thermogravimetric analysis (TGA). Often, the onset of the mass loss during thermal scan is used as a measure of thermal stability [31–34]. In our last study, we have shown that this descriptor is irrelevant to thermal decomposition and thermal stability, and that a concept like “decomposition temperature” doesn’t have any theoretical background [35,36]. It was shown that TGA studies carried out with open crucible and in scanning mode can be significantly affected by evaporation of the studied system. However, by applying a sealed crucible with tiny orifice, the vaporization process can be suppressed, and the mass loss rate will correspond to only the decomposition process. The method of isoconversional kinetics can provide the kinetic parameters [37]. This method employs the temperature shift of the mass loss dependent on the heating rate. In such conditions, the decomposition pathways can be separated by changing the heating rate. Such an approach is often applied for the determination of the melting properties of biological compounds [37–42]. By analyzing the temperature dependence of decomposition mass loss with the method of isoconversional kinetics [43,44] one can evaluate the decomposition activation energy (E_A) and frequency factor ($\ln A$). However, the kinetic parameters of decomposition cannot shed much light on the chemical processes that take place during decomposition or provide deeper insight since the overall decomposition combines all possible reaction pathways.

Decomposition of [C₂Mim][OAc] was already studied by Cao [32] and Clough [21]. In both studies mass loss rates were recorded in isothermal conditions in crucibles with the sample surface opened to the purge gas. In both studies the E_A determined using TGA ranges from 110 to 115 kJ mol⁻¹. Computations using dispersion- and counterpoise-corrected B3LYP yielded higher barriers for decomposition S_N2 and E2 pathways of 136 – 157 kJ mol⁻¹ in the gas phase. It is hard to separate all these processes during the mass loss rate data treatment. Clough *et al.* [21] tried to rationalize the activation energies E_A observed in experiments by accounting for acetic acid and carbene structure formation as the transition state. But the activation energy of this decomposition pathway was found

to be significantly lower ($E_A = 80 \text{ kJ mol}^{-1}$) than the experimental values. Finally, Clough summarizes that S_{N2} is the most preferred decomposition pathway, but the observed discrepancy in activation energies remains open.

In this study, we apply the method of isoconversional kinetics together with approaches suppressing the vaporization mass loss rate to determine the decomposition kinetic parameters for $[\text{C}_2\text{Mim}][\text{OAc}]$. In addition, we provide molecular level insight into the various decomposition pathways with the help of high-level quantum chemical computational analysis.

2. Methods

Chemicals

The sample of $[\text{C}_2\text{Mim}][\text{OAc}]$ was purchased from Io-li-tec GmbH. The initial mass purity of the sample was 0.98 according to the supplier specifications. $[\text{C}_2\text{Mim}][\text{OAc}]$ is a highly hygroscopic, which can lead to an additional mass loss step near 380 K corresponding to vaporization of volatile impurities in the sample if no *in situ* pre-treatment was carried out. Therefore, the sample was put under vacuum for 5 h at 333 K at residual pressure of 100 Pa. Additionally, the sample was *in situ* purified by exposing to the stream of dry nitrogen gas (dew point is lower than 160 K) at 370 K for 10 minutes. After such purification no mass loss prior to decomposition was observed during TGA studies.

Thermogravimetric analysis

The detailed description of the isoconversional TGA study of decomposition kinetics for ionic liquids is given in a recent publication [35]. Concisely, 3 to 5 mg sample of $[\text{C}_2\text{Mim}][\text{OAc}]$ was put in an aluminum crucible either with the sample's surface opened to nitrogen purge gas or sealed by a lid with a tiny orifice of 20 to 30 μm diameter. The samples were heated with different constant rates from 0.1 to 10 $\text{K}\cdot\text{min}^{-1}$. The mass of the sample was recorded during heating from 303 to 873 K in a Perkin Elmer TGA 6 device.

The experimental study with open crucible in most cases corresponds to the simultaneous evaporation and decomposition processes. In the case of tiny orifice, we expected (based on simulations described below, cf. Fig. 3 and its discussion) the evaporation process to be suppressed to great extent and decomposition to be the main source of the observed mass loss.

Kinetic parameters describing this mass loss are casted into the "kinetic triplet", consisting of activation energy E_A , frequency factor A , and the kinetic model. The choice of the kinetic model may thus affect the other two parameters, mostly the frequency factor. We analyzed our data to estimate the impact of the choice of the kinetic model on the derived parameters, in particular the mass loss α over time t with several models. Linear regression was carried out with THINKS using the reduced Sestak-Berggren equation [45]. With this method, the kinetic model can be determined based on the model parameters n and m without the assumption of a concrete reaction model [46]. The underlying formula reads

$$\ln\left(\frac{d\alpha}{dt}\right) - \ln[(1 - \alpha)^n \alpha^m] = \ln(A) - \frac{E_A}{RT} \quad (1)$$

When m is assumed to be zero, the method of isoconversional kinetics can be used to determine the activation energy for arbitrary n (in this case, n would correspond to the order of reaction). This approach is therefore often called model-free analysis [44]. We analyzed our data by fitting n , m , A ,

and E_A as well as assuming an ordinary first-order process by setting $m=0$, $n=1$, determining E_A from isoconversional kinetics, and fitting A . The detailed description of the isoconversional procedure can be found in our recent publication [35] and in the book of Vyazovkin [44].

Computations

Ab initio computations in this project comprise DFT geometry optimizations (and scans) and frequency computations, single-point energy coupled-cluster calculations, and COSMO calculations. Statistical mechanics calculations to obtain thermodynamic and kinetic data involve one-dimensional hindered rotor (1DHR) corrections, solvation modeling with COSMOtherm, and transition state theory (TST) rate constant calculations.

Geometries and frequencies have been computed using the gaussian16 b.01 software [47] at the DFT PW6B95D3/6-311++G(d,p) level of theory. We applied very tight SCF convergence criteria and an extremely fine integration grid (199 radial shells and 974 angular points per atom). Starting points for conformer optimizations were taken from Clough *et al.* [21], *cf.* Fig 8, and from CREST simulations [48]. Single-point energies (SPE) at delocalized pair natural orbital approximated (DLPNO) CCSD(T)/aug-cc-pV(T,Q)Z level of theory were computed with ORCA 4.1.2 [49]. The extrapolation with augmented triple- and quadruple ζ Dunning basis sets was done according to the formula provided by Liakos *et al.* using $\alpha = 5.79$ and $\beta = 3.05$ [50,51]. For all DLPNO calculations, TightSCF and TightPNO settings were used. Ideal-gas Gibbs free energies using the RRHO and the 1DHR model, see below, were computed using TAMkin [52]. Free energies of solvation were computed using the COSMOthermX software version 19.0.1 [53–56]. The corresponding COSMO calculations were performed with Turbomole 7.1 [57] at BP86/def-tzvp level.

Reaction rate constants in the ideal gas state $k_{i,G}$ were computed with conventional TST [58] with Eckart tunneling in the ideal gas state using the python package Tamkin [52]. Using TAMkin, we performed quantum-mechanical one-dimensional hindered rotor (1DHR) treatments around the $C_2Mim - OAc$ axis. To obtain the corresponding potential energy curve, scans were performed in Gaussian in 5° or 10° steps with the same method as that used for geometry optimization. Then, in TAMkin, 2000 basis functions were used to solve the 1D-HR Schroedinger Equation. Our in-house code TamkinTools [59] was used to obtain very smooth Fourier series fits to the potentials by not only minimizing the RMS deviation from the computed points but also minimizing the curvature. This lets us use Fourier series of higher order to obtain better fits while still avoiding oscillations.

Rate constants for the liquid phase are calculated according to the work of Gertig *et al.* [60 and supporting information, Eq. S25]:

$$k_{solv} = k_{i,G} \exp\left(-\frac{\Delta G_{solv,TS} - \sum(\Delta G_{solv,i})}{RT}\right) \quad (2)$$

Ionic liquids, the reactant, may be modeled either as separated ions (a 1:1 mixture of anions and cations) or as one substance composed of the ion pair complex. In this study, both views are employed and compared. Rate constants were calculated as bimolecular reactions in the separated-ions view, and as well as unimolecular reactions in the ion pair complex view.

We incorporated the Gibbs free energies of solvation into the rate and equilibrium constant calculations with a linearly temperature-dependent model. This linear approximation may lead to errors of $2 \text{ kJ}\cdot\text{mol}^{-1}$ over the temperature range used here.

3. Results

Experimental Results

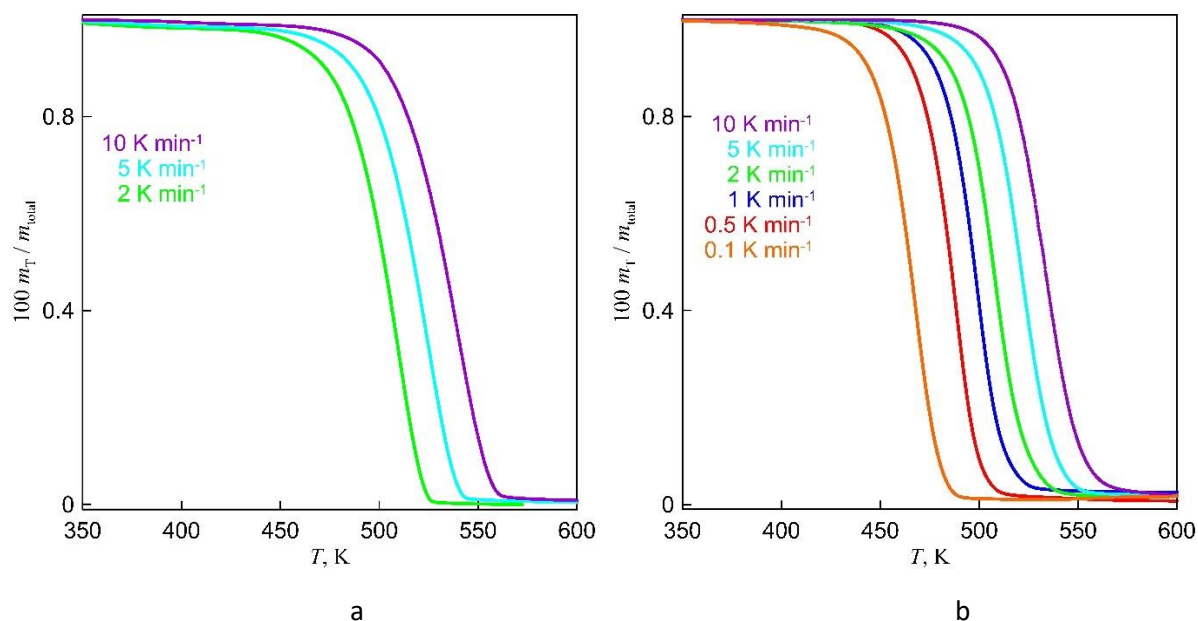


Fig 1. Temperature dependence of mass of $[\text{C}_2\text{Mim}][\text{OAc}]$ sample from (a) the open surface and (b) through tiny orifice in pan's lid.

Fig. 1 shows the temperature dependence of the mass recorded in our TGA device with (a) open crucible and (b) sealed crucible with a tiny orifice in the lid. The temperature interval in which the mass loss takes place is wider for the case of the open surface (a) than for the closed crucible with the tiny orifice (b), compare for the steeper slope in (b). The mass loss was corrected for the mass change of the empty cell on heating with the corresponding heating rate. From the corrected time / temperature dependence of the sample mass the rate of mass loss was evaluated and presented in Fig. 2.

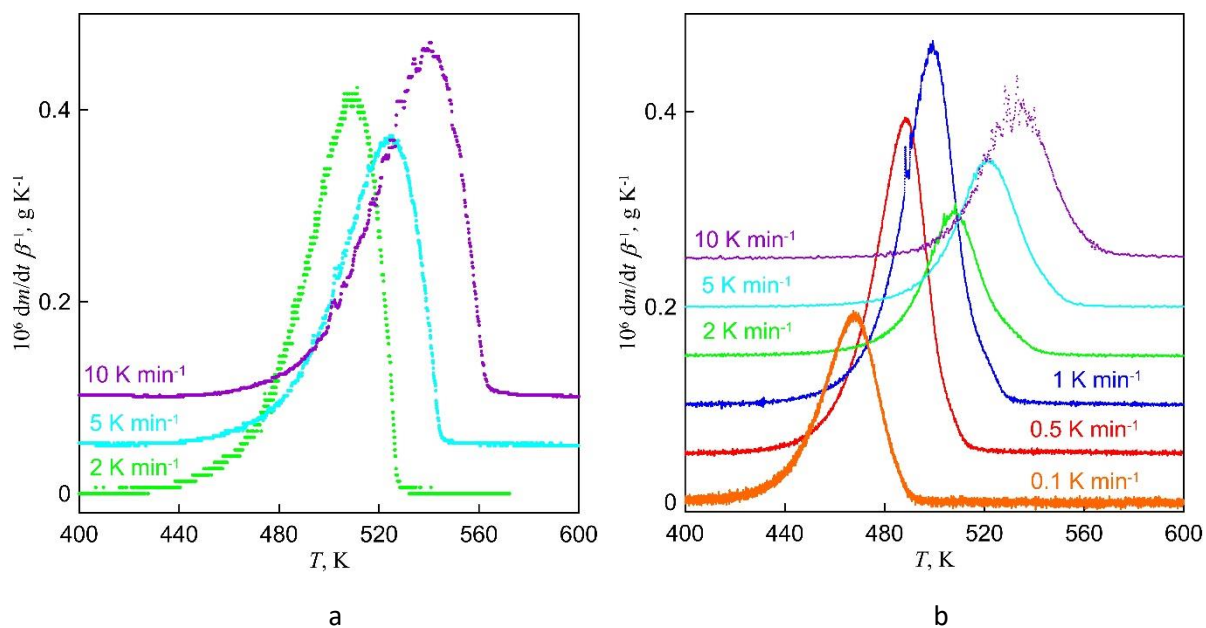


Fig 2. The temperature dependence of mass loss for [C₂Mim][OAc] from (a) open crucible, (b) through tiny orifice in the lid of sealed DSC pan. For illustration purpose the mass loss rates are shifted by $5 \cdot 10^{-8} \text{ g} \cdot \text{s}^{-1}$ step.

As it was shown by simulations using the formal kinetic background in the previous publication [35], the shape of the mass loss curve can be used as an indirect proof of evaporation contribution into the mass loss of the sample during study. A purely chemical transformation should show a bell shape, while an evaporation process leads to an exponential growth of the mass loss rate with rather fast decrease after maximum peak due to the depletion of the sample in the crucible (see Fig. 3). For the open crucible (Fig 2a), the temperature dependence of mass loss shows characteristic features of evaporation process: the left side of the peak corresponds to exponential increase in mass loss and the right side of the peaks shows the steep drop in mass loss, what corresponds to fast sample depletion due to evaporation process. In contrast, for the tiny orifice (Fig. 2b), the temperature dependence of the mass loss shows symmetric peaks corresponding to an increase and decrease of the reaction rate with change in the reactant volume / mass / number during the time/temperature profile of the chemical transformation. Comparison with simulated mass losses reported previously [35] (cf. Fig. 3) indicate that determination carried out with the opened crucible consist to large degree of evaporation process in the total mass loss.

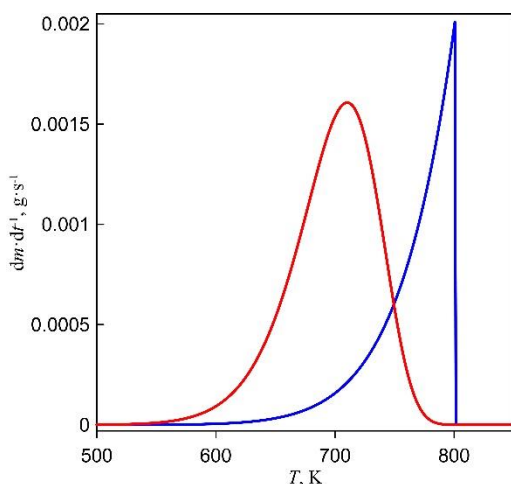


Fig. 3. The simulated mass loss in the TGA apparatus due to vaporization (blue line) and decomposition (red line). Two-thirds of the initial mass of the sample is left after decomposition study. The simulation parameters are $\Delta_f^{\ominus}H_m^{\ominus} = E_A = 120 \text{ kJ} \cdot \text{mol}^{-1}$, $\ln A = 15$, $p_{\text{sat}}(298.15 \text{ K}) = 10^{-9} \text{ Pa}$. (Copied with permission of Elsevier from [35])

We have analyzed the mass loss for both cases (open surface and tiny orifice) in terms of isoconversional kinetics. The resulting activation energy dependence on the [C₂Mim][OAc] conversion is presented in Fig. 4. A first-order process is assumed to also fit the frequency factor A .

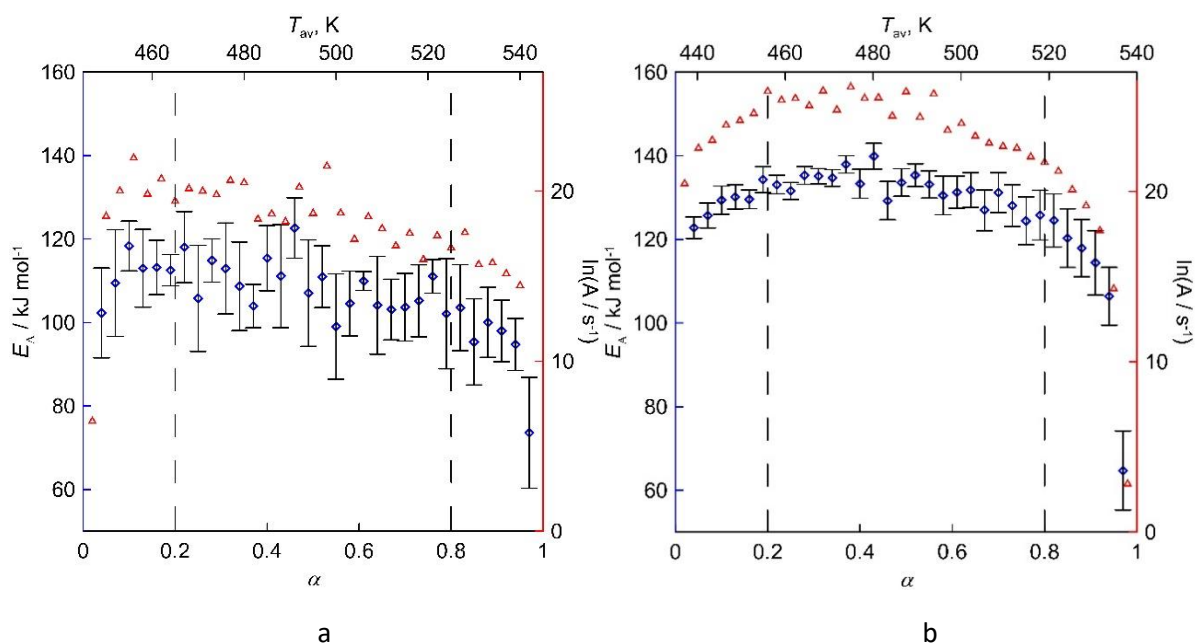


Fig. 4. The conversion dependence of activation energy E_A and frequency factor $\ln(A)$ for $[\text{C}_2\text{Mim}][\text{OAc}]$ in TGA study: (a) in crucible with the sample surface opened to purge gas, (b) in sealed pan with tiny orifice in the lid. Vertical dashed lines limit the region of α preferred for analysis. The error bars correspond to standard deviation with 0.68 level of confidence (1σ).

It is recommended to avoid analyzing the activation energies E_A and frequency factors $\ln A$ for low values of conversion ($\alpha < 0.2$) and above $\alpha = 0.8$. In the mentioned regions the results are easily affected by volatile impurities and changes in physical properties of the reaction mixture. The data in Fig. 4 show that the sealed pan leads to processes with an activation energy approximately 20 to 25 $\text{kJ}\cdot\text{mol}^{-1}$ higher than for the processes with the opened crucible. In both cases, in the interval of α from 0.2 to 0.8, the E_A and $\ln A$ values can be treated as constant values within the experimental determination uncertainty; they are given in Table 1. In addition to the observed shapes of the mass loss curves, the difference in activation energies supports the idea that the TGA study with the opened sample surface is significantly affected by the vaporization mass loss. The activation energy for the open surface corresponds to what one would expect for $[\text{C}_2\text{Mim}][\text{OAc}]$ enthalpy of vaporization. We have not been able to find experimental values for $[\text{C}_2\text{Mim}][\text{OAc}]$ enthalpy of vaporization, but Pliego *et al.* report enthalpies of vaporization for $[\text{C}_4\text{Mim}][\text{OAc}]$ and $[\text{C}_6\text{Mim}][\text{OAc}]$ and from that one could estimate the enthalpy of vaporization for $[\text{C}_2\text{Mim}][\text{OAc}]$ to be about $120\text{ kJ}\cdot\text{mol}^{-1}$ [61]. Also, from the temperature dependence of our calculated Gibbs free enthalpies of solvation calculated in subsection “Computational Results”, one can derive the enthalpy of vaporization using a Gibbs-Helmholtz relationship to amount to $110\text{ kJ}\cdot\text{mol}^{-1}$. These findings indicate that TGA experiments with an open surface merely measure vaporization.

Table 1. The evaluated E_A and $\ln A$ for $[\text{C}_2\text{Mim}][\text{OAc}]$ under experimental conditions of TGA technique.^a

IL	Opened surface		μm size orifice	
	$E_A, \text{kJ}\cdot\text{mol}^{-1}$	$\ln(A / \text{s}^{-1})$	$E_A, \text{kJ}\cdot\text{mol}^{-1}$	$\ln(A / \text{s}^{-1})$
$[\text{C}_2\text{Mim}][\text{OAc}]$	110 ± 9	19 ± 1	135 ± 2	25 ± 0.5

^a the standard deviation with confidence level 0.68, $k = 1$ is presented as uncertainty

The mass loss rate for the sealed pan with tiny orifice correlates with the IL decomposition reaction. The evaporation process with low activation energy leads to the IL gas phase filling up the remaining space in the pan not filled by the liquid. For comparably low heating (and therefore evaporation)

rates and low outflow rates (due to the tiny orifice), the concentrations in the gas phase can be assumed to be in steady state. Then, the outflow and the mass loss rate (lowering product concentration) equal the gas decomposition rate (increasing product concentration).

To evaluate the influence of the reaction model onto activation energy and frequency factor, we fitted a general model, i.e. with variable reaction orders n and m , according to Eq. 1. If the entire series of measurements is used, the fit used predicts an activation energy of $136.5 \text{ kJ mol}^{-1}$, a frequency factor $\ln A$ of 30.3, and a reaction order of $n=1.20$. The other order parameter m amounts to almost zero. Still, the lack of fit is high, possibly by further processes influencing the measurement. The deviation is particularly predominant for the highest and lowest temperatures. For the investigated system, the non-instantaneous evaporation could cause deviations from the real decomposition rate at low temperatures. At very high conversions, the decomposition products may react in some way and change the kinetics of mass loss. These effects are removed by limiting the conversion to the range between 0.2 and 0.8. We further set $m=0$ as found out from the previous fit. The kinetic parameters thus obtained are $133.8 \pm 1.0 \text{ kJ mol}^{-1}$ and $n=0.83$ (Fig. 5).

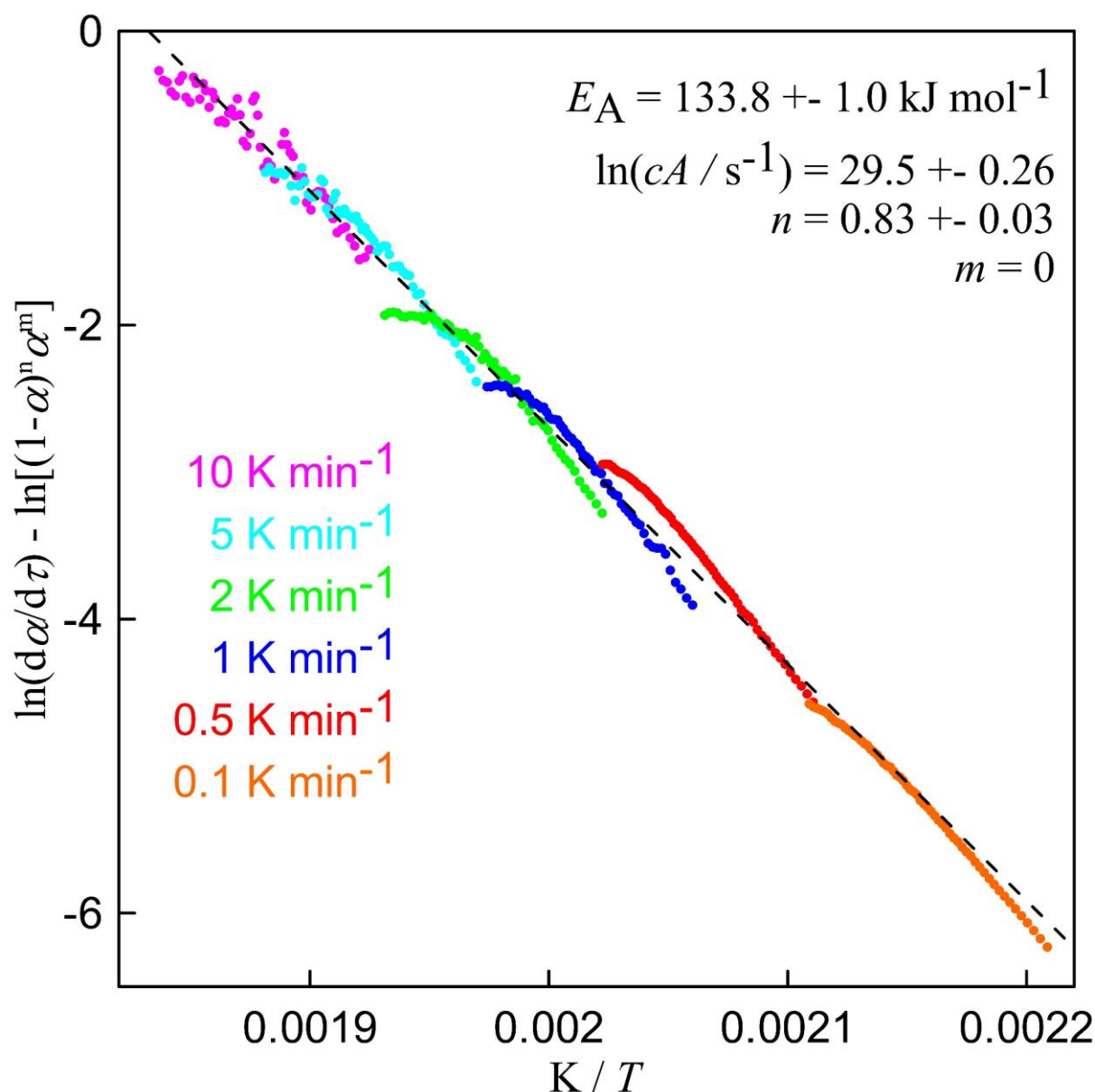


Fig. 5 Fitting the experimental mass loss with Sestak-Berggren equation [45] over interval of IL conversion from 0.2 to 0.8, setting $m = 0$ and adjustable n .

This agrees well with the activation energy from the DFT calculations by Clough and this study (see subsection “Computational Results”), and is close to the expected reaction order of one for the proposed unimolecular IL decomposition mechanisms. Non-integer reaction orders are not uncommon when investigating the thermal stability of ionic liquids [62]. Although evaporation effects were significantly reduced by the experimental set-up used, it can be speculated that these could still be present on the reaction order that was obtained.

In order to obtain parameters for a simpler model of integer order, we assumed a first-order reaction with $m=0$ and $n=1$ and with instantaneous evaporation of the decomposition products since this comes closest to the non-integer parameters from the previous paragraph. The fit to the measured data yield a slight change in activation energy to 135.3 ± 1.2 kJ mol, cf. Fig. 5 and Table 1.

In contrast, previous studies using a constant heating rate or an isothermal approach showed significantly lower activation energies of 112.6 kJ·mol⁻¹ [32] and 116 kJ·mol⁻¹ [21]. We conclude that a combination of decomposition and evaporation was measured there, and that the methodology presented in this study allows for the isolation of decomposition reactions.

Computational Results

Experiments like TGA can only determine the total decomposition rate, not the type of reaction involved. *Ab initio* calculations can yield rate constants of specific reactions so that one may compare which pathway has the largest contribution to the total rate constant and which slope, *i.e.* activation energy, best matches the experimental observations. Transition State Theory (TST), according to Eq. 2, yields reaction rate constants when the energies, entropies, and possibly solvation effects are known for the respective barriers and reactants.

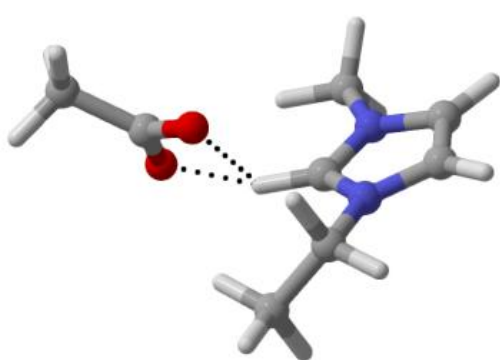


Fig 6a: $\chi=249^\circ$, lowest DFT energy. Ethyl group and acetate lean to the same side.[63]

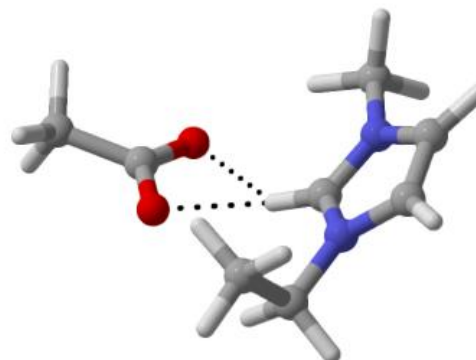


Fig. 6b: $\chi=60^\circ$, lowest CC energy. Ethyl group and acetate lean to opposite sides.[63]

For the [C₂Mim][OAc] reactants, different conformations exist arising from different orientations of the cation and the anion, affecting reactant energy and entropy. The torsional angle between anion and cation could be defined by χ : (central C₂Mim C) – (N adjacent to methyl) – O – O. It can also be done by θ : (central C₂Mim C) – (N adjacent to ethyl) – O – O. The ethyl group torsion may also couple to that motion. In forward and backward scans of χ , we obtained four conformations, while the profile for θ showed only 2 different minima (and a rotational symmetry of 2). All profiles, in particular those for χ , showed sharp jumps that stem from coupling to other motions. A one-

dimensional hindered rotation (1DHR) scheme thus cannot fully account for the coupled movement of the OAc and the ethyl group rotations. The two lowest-energy conformations differ by the position of the acetate to be either on the same side of the imidazole group as the ethyl group (lowest DFT energy, Fig. 6a) or in plane with the imidazole group (second-lowest energy, Fig. 6b). Higher-level energy calculations using DLPNO-CCSD(T) lead to the energetic order of these conformations swapping so that the 0° conformation from Fig. 6b is 0.2 kJ/mol lower than the Fig. 6a conformation.

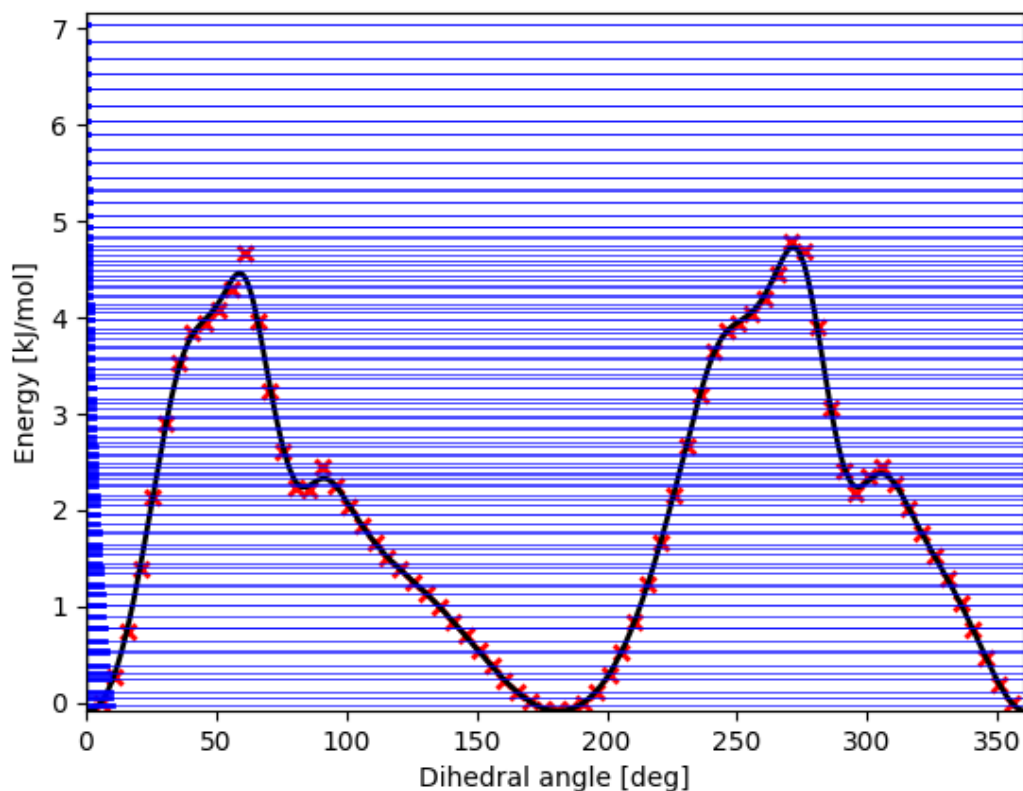


Fig. 7 The potential energy surface of acetate rotation around the central-C – ethyl-N – O – O dihedral angle θ in $[C_2Mim][OAc]$. Red crosses are DFT geometry optimizations from a scan, the black curve is the potential energy fit, and the blue horizontal lines correspond to energy levels from solving the torsional Schrödinger Equation.

We base our calculations on this scan since it refers to the global minimum on the DFT method used for the scan.

Table 2. Evaluated coupled-cluster energy differences (barriers and reaction energies with respect to the ion pair complex reactant) without (ΔE_{CC}) and with vibrational zero-point energy ($\Delta E_{CC,ZPE}$). The last row lists Gibbs free energies of solvation of reactants, transition states, and products

<i>Reactants</i>	ΔE_{CC} , kJ·mol ⁻¹	$\Delta E_{CC,ZPE}$, kJ·mol ⁻¹	$\Delta G_{m,solv}^{\circ}$ (473K), kJ·mol ⁻¹
ion pair complex ^a	0	0	-65,85
separated ions	429.8	425.6	-361,7
<i>Barriers</i>			
S _N 2 Methyl	143.4	138.7	-48.6
S _N 2 Ethyl	145.4	139.9	-49.0
E2 anti (wide)	179.8	162	-49.4
E2 syn	165.8	154.4	-36.4

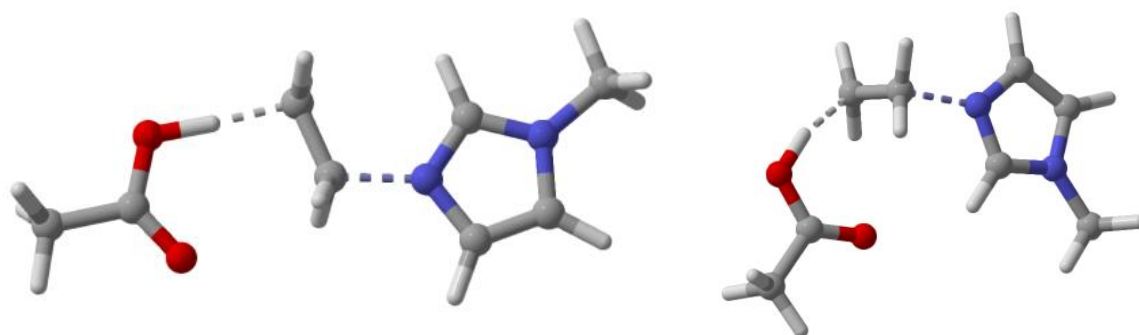
Products

C ₂ Im + C ₁ OAc	-10.4	-13.9	-33.9
C ₁ Im + C ₂ Oac	-14.0	-18.2	-34.6
C ₁ Im + C ₂ H ₄ + HOAc	61.5	43.5	-42.4

^a ion pair complex is taken as a reference for ΔE_{CC} and $\Delta E_{CC,ZPE}$ calculation

The hindered rotation of the anion versus the cation is also present in the transition states. It is treated equivalently to the reactant ion pair complex within a one-dimensional approach using TAMkin and our TamkinTools extension.

As an example for hindered rotor treatments and conformations of the transition states in this study, we briefly discuss the interesting case of anti-elimination. Here, the scan reveals two lower minima of almost same depth at 0° and 170° and a slightly higher minimum at 70°, depicted in Fig. 9.



(a) lowest-DFT-energy conformation with $\theta = 170^\circ$

(b) 2nd-lowest-DFT-energy conformation with $\theta = 0^\circ$

Fig. 8 The geometry of the transition states for the anti-elimination pathway, with dihedral angles θ as central-C – ethyl-N – O – O [63]

The minimum at 0° dihedral angle is 0.07 kJ·mol⁻¹ higher than the minimum at 170° for DFT. At DLPNO-CCSD(T), it is instead deeper by 1.3 kJ·mol⁻¹. Moreover, the 0° minimum is considerably wider as can be seen from Fig. 9, which usually leads to an entropy contribution dominating free energies. Because of these virtually equal energies, we made an exception for just this case and used the slightly higher, but far wider, conformation at 0° upon which to base the TAMkin calculation. While the energies of the two minima are almost equal, using the one with higher entropy will lead to more realistic results. Hindered rotor correction factors are highest for the anti-elimination rate constant and range from 4.1 to 4.3. All HR corrections in this study show very little temperature dependence.

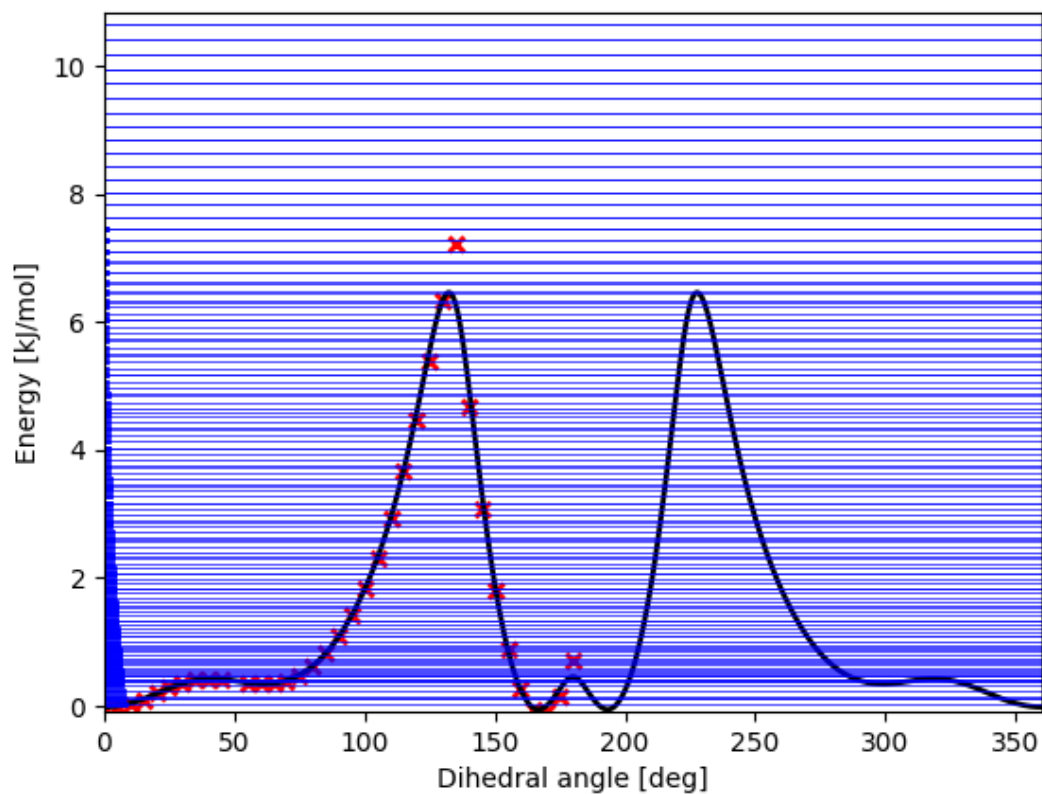


Fig. 9: Potential energy surface for hindered rotation around central-C – ethyl-N – O – O dihedral angle. Plot details same as Fig. 7. Because this one-dimensional hindered rotor possesses mirror symmetry, potential energies were only calculated for points between 0° and 180° and even symmetry was imposed on the Fourier fit.

We report computed gas and liquid phase rate constants for substitution at the methyl and ethyl groups and the syn- and anti-elimination, *i.e.* S_N2 and E2, rate constants. Parameters of the Arrhenius fit to computed rate constants are reported in Table 3.

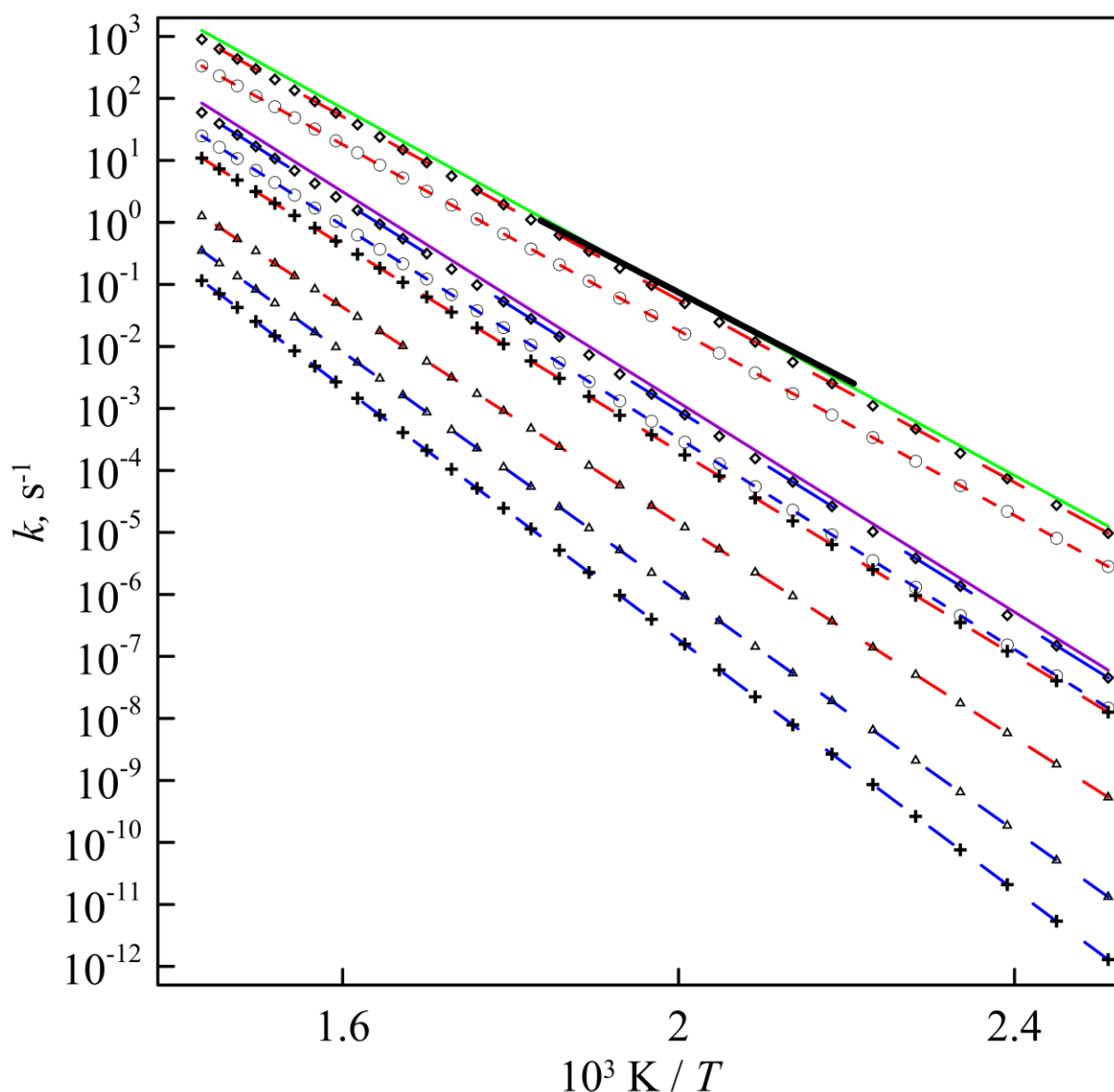


Fig. 10: computed unimolecular rate constants for IL decomposition compared to the experimental rate constant (black solid line) obtained as in Fig. 5. The calculations include gas-phase tunneling and hindered rotor effects. Two substitutions (circles \circ at methyl group and diamonds \diamond at ethyl group) and two eliminations (triangle Δ for syn- and plus $+$ for anti-elimination) are shown explicitly for the ideal gas and the COSMO-RS liquid state (lower lines, same symbols). The green continuous line amounts to the total rate constant as sum of all gas-phase pathways, the violet continuous line to the total rate in the liquid phase.

Figure 10 shows that gas-phase substitution largely coincides with the observed process (analyzed as first-order reaction). S_N2 substitution pathways are considerably faster than other reaction types. Gas-phase rate constants are also higher than the ones in the liquid phase, which have been modeled to account for COSMO-RS free energies.

As pointed out in the method section, one may think of the liquid phase in two different ways: as being composed of two separate ions or as being composed of ion pair complexes. Accordingly, one may model the reactant either as being made up of a 1:1 mixture of separately calculated ion species or as a pure substance of complexes. In addition to the complexes that we explicitly modeled above, we also computed properties for the separate ions to compare both reactant models. The reaction order for the 1:1 mixture case would naturally be 2 for the bimolecular reactants (cation and anion).

These rate constants need to be multiplied by the ion concentration $c(T, p=1 \text{ bar})$ in order to be compared to unimolecular rate constants inferred from experiments. In total, one can compare up to 8 combinations: the reactants modeled as either separate ions or as ion pair complex, dissolved in either separated ions or in pure ion pair complexes, and expressed as either a uni- or bimolecular rate constant. None of the combinations yield liquid phase rate constants with activation energies or rate constants close to the experimental ones from Figure 5, cf. Fig. 12.

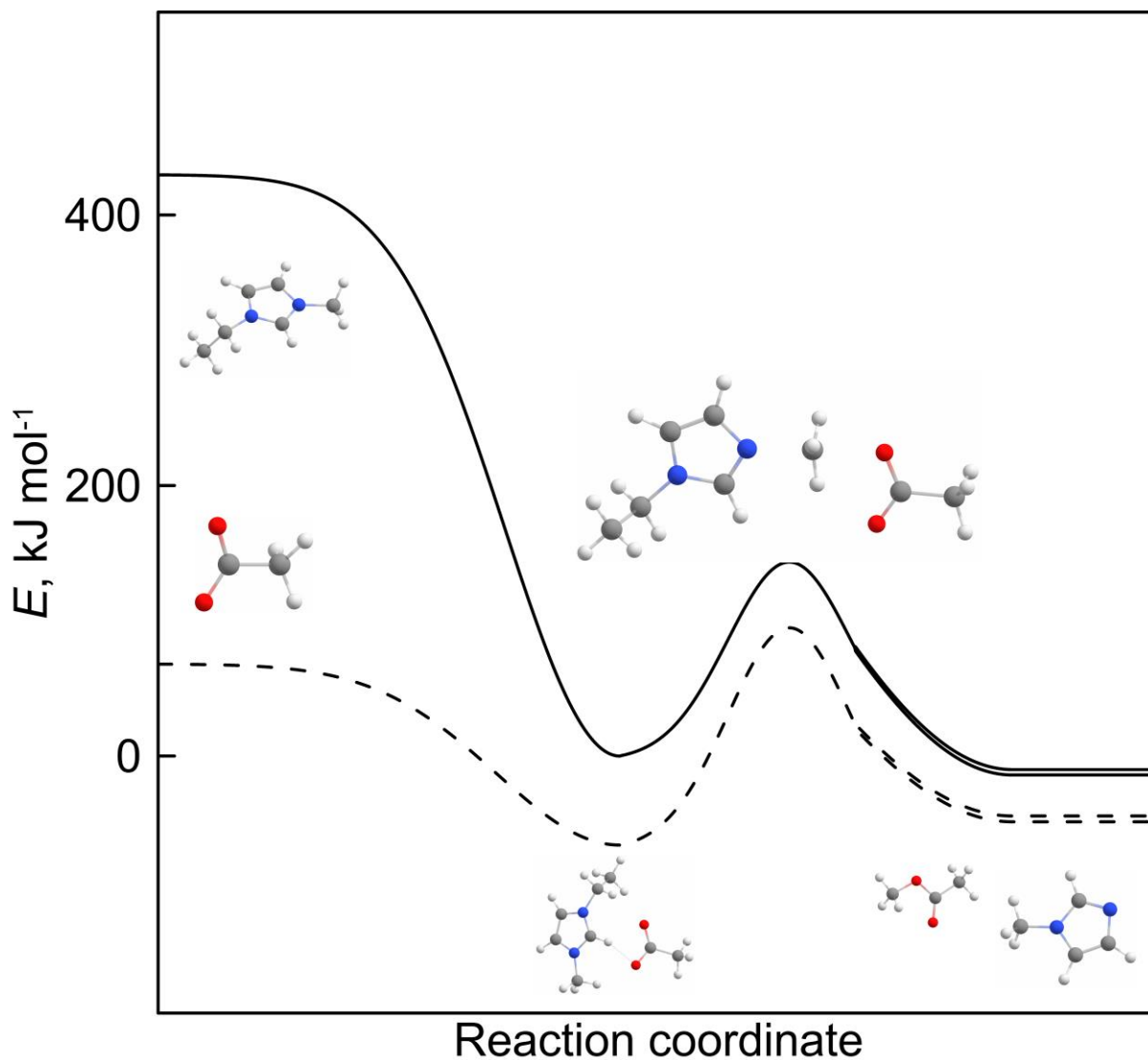


Fig. 11: Potential energy scheme with reactants modeled as separated ions or as ion pair complex. Only the lowest-energy S_N2 decomposition pathway is given. Solid lines refer to coupled-cluster potential energies, dotted lines to energies corrected for Gibbs free energy of solvation.

Using the ideal gas reference for the separate ions is computationally difficult because they are higher in energy than the transition states due to the missing “liquid cage” stabilization and charge transfer in the liquid, cf. Fig. 12. Within the TAMkin software, one cannot simply evaluate the gas-phase TST data for negative potential energy barriers and afterwards apply liquid-phase corrections. Therefore, we factor out a bias energy, E_{bias} , like so

$$k(T) = \frac{k_B T}{h} \exp\left(-\frac{G_{\text{TS}} - G_{\text{react}}}{RT}\right) = \frac{k_B T}{h} \exp\left(-\frac{G_{\text{TS}} - G_{\text{react}} - E_{\text{bias}}}{RT}\right) \exp\left(-\frac{E_{\text{bias}}}{RT}\right)$$

We modify the bias of the gas-phase data for the separate ions so that it matches that of the ion pair complex. We then apply liquid-phase corrections, and correct the resulting rate constants for the bias. This can slightly affect tunneling calculations but these here yield negligible effects anyway).

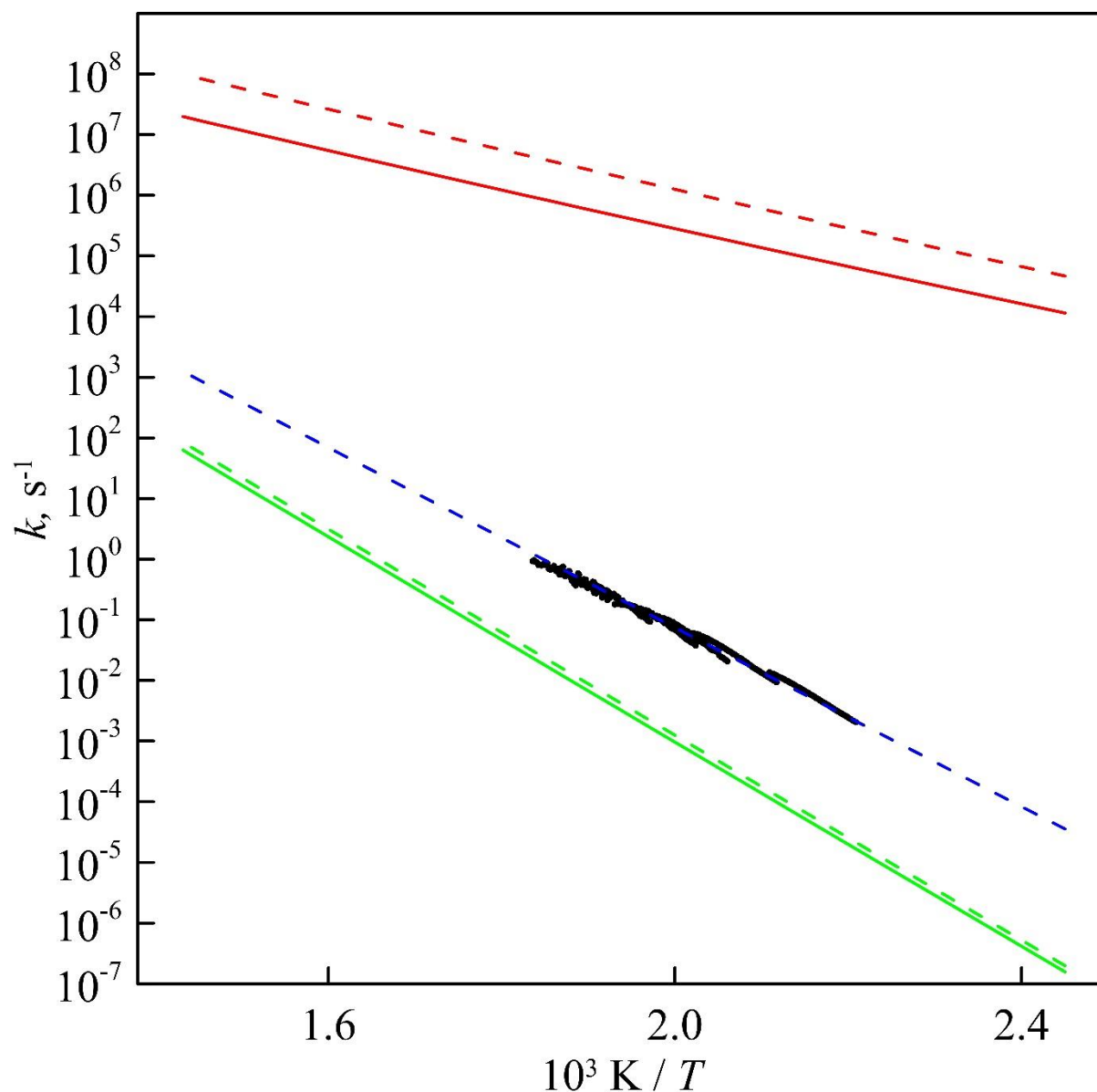


Fig. 12: Rate constant comparison for different models of the reactant in the liquid phase. Black points show TGA experiment data for the total decomposition rate constant in this study. The middle dashed blue line shows ab initio TST rate constants for the sum of all gas-phase reactions. The lower lines (green) show this sum with solvation corrections for the ion pair complex solvated in ion pair complexes (dashed) and in the separated ions (solid). The upper lines (red) show the sum for the bimolecular separated ion reactants in separated ions (solid) and in the ion pair complexes (dashed). The bimolecular rate constants have been multiplied by $[C_2Mim][OAc]$ concentration from experiments by Królikowska et al [64] to compare them to unimolecular rate constants.

Figure 12 shows total $[C_2Mim][OAc]$ decomposition rate constants (i.e. the sum of all substitution and elimination reactions) for the gas phase and for four solute-solvent combinations. The measurement data from this study match the total gas phase data – dominated by S_N2 methyl group substitution – very well, both in slope and offset. For liquid phase reactions, neither is true: with the ion pair complex as educt, rate constants are 2 orders of magnitude too slow and slightly more temperature-

dependent. With the separated ions as reactants, rate constants are much too high and much less temperature-dependent. They have been multiplied by the IL concentration (in the order of 5 to 6 mol·l⁻¹). The choice of solvent does not have much influence on rate constants, be it the ion pair complex or the separated ions. In general, continuum solvation models tend to provide insufficient solvation energy for ions as shown by Pliego *et al.* [61] what renders reaction rate constants from separated ion reactants too fast when reacting via a neutral TS.

For entropic reasons, the real liquid phase will be made up neither completely of complexes nor completely of separated ions: it will be a mixture or superposition of both. The overall reaction rate constant in liquid phase, taking the formation of pre-reaction complexes or pairs into account, might behave in a way that is between the limiting cases of Fig. 12 and eventually come closer to the experimental data.

Table 3: Arrhenius parameters of computed reaction rate constants by TST with Eckart tunneling and 1D HR at DLPNO-CCSD(T)/aug-cc-pV(T,Q)Z//PW6B95D3/6-311++G(d,p) level of theory.

Pathway	A, s ⁻¹	E _A , kJ·mol ⁻¹
Gas phase		
S _N 2 Methyl	3.67E+13	142
S _N 2 Ethyl	1.88E+13	144
E2 anti	1.01E+13	166
E2 syn	8.21E+12	159
Liquid phase		
S _N 2 Methyl	8.33E+13	163
S _N 2 Ethyl	4.77E+13	165
E2 anti	2.69E+13	187
E2 syn	4.05E+13	195

Table 4: vapor-liquid equilibrium data for reactants and products from COSMOtherm (in ion pair complex solvent (critical temperature for methyl acetate 506 K, for ethyl acetate 530 K)

Substance	$p_{\text{sat}}(473.15 \text{ K}), \text{ mbar}$	$p_{\text{sat}}(573.15 \text{ K}), \text{ mbar}$	$\Delta H_{\text{vap}}(473.15 \text{ K}), \text{ kJ}\cdot\text{mol}^{-1}$
[C ₂ Mim][OAc]	0.0115	0.919	100.7
Methyl Imidazole	493	3.3·10 ³	42.3
Ethyl Imidazole	393	2.8·10 ⁴	43.9
Acetic acid	1.03·10 ⁴	4.33·10 ⁴	46.6
Methyl Acetate	1.92·10 ⁴		24.0
Ethyl Acetate	1.13·10 ⁴		26.7

Along with the Gibbs free energy of solvation calculations (cf. Table 2), we calculated vapor-liquid equilibrium data shown in Table 4. These confirm that the IL decomposition products are highly volatile while the IL has negligible vapor pressure. Nevertheless, larger imidazolium products especially may remain in the liquid phase in low concentrations. The activation energy in the gas phase is lower by approximately 20 kJ·mol⁻¹ than the liquid phase, which renders gas-phase decomposition rate constants roughly a factor of 100 ... 1000 faster. On the other hand, the

concentration of IL in the gas phase may only be on the order of 1 promille. Taking into account the quite large uncertainties for the modeling of the liquid phase, no final decision on the dominant process can safely be made. A detailed analysis, *i.e.* a reactor model, of the different phases with finite concentrations, though, requires solving time-dependent differential equations for both gas and liquid phase (as done by Gertig et al. [60]) that take vapor-liquid equilibria and forward and reverse reactions into account.

Conclusions

Earlier reported activation energies of around $110 \text{ kJ}\cdot\text{mol}^{-1}$ based on mass loss measurements with an open orifice could be confirmed neither by the calculations nor by the measurements of this study. None of the computationally investigated reaction pathways showed an activation energy close to, e.g. within 20 kJ/mol of, such low values. Measurements in the open pan therefore do not display decomposition chemistry. They are rather influenced by vaporization kinetics, as illustrated by the model in Fig. 3. and also agree with calculated enthalpies of vaporization from this study.

TGA experiments from this study can be well interpreted with a unimolecular reaction model, which yields an observed activation energy of 135 kJ/mol . This fits best to substitution reactions in the gas phase, predominantly at the methyl group. The total rate constant computed for the gas phase, *i.e.* the sum of substitutions and eliminations, very closely matches the rate constant inferred from the experiments. Our calculations also account for tunneling in the gas phase, but this is of minor influence on rate constants with factors below 1.2. Hindered rotation, in turn, is always considered and lowers the rate constants by factors of 2 to 3.

Rate constants for the liquid phase computed with Gibbs free energies of solvation using COSMOtherm considerably differ in magnitude and slope from the experiment. In practical applications nevertheless, the lower rate constants in the liquid phase can still dominate long-term degradation processes. Uncertainties in the rate constant computations for the liquid phase most likely stem from solvation models for the reactant. Different solvent models for the reactant (ion pair complex or separated ions) yielded strongly varying rate constants, some larger and some smaller than the gas-phase ones (all of which had slopes that were very different from experimental observations and gas-phase substitutions). A better solvation model, like a cluster-continuum model, or thermodynamic integration would be a step forward to correct liquid-phase rate constants that could be between the two cases shown in Fig. 12 and closer to the experimental findings. Also, a detailed time-dependent modeling of the two-phase multicomponent reactor that includes the vapor-liquid equilibrium of all species and their forward and backward reactions in gas and liquid, as well as effusion from the pan, could more realistically reproduce the experiments.

Acknowledgements

Simulations were performed with computing resources granted by RWTH Aachen University under project rwth0070 and thes0754. We acknowledge funding by DFG for project 407078203.

References

- [1] E. Fabre, S.M.S. Murshed, A review of the thermophysical properties and potential of ionic liquids for thermal applications, *J. Mater. Chem. A*. 9 (2021) 15861–15879. <https://doi.org/10.1039/D1TA03656D>.
- [2] Y.U. Paulechka, A.G. Kabo, A. V Blokhin, G.J. Kabo, M.P. Shevelyova, Heat capacity of ionic

- liquids: Experimental determination and correlations with molar volume, *J. Chem. Eng. Data*. 55 (2010) 2719–2724. <https://doi.org/10.1021/je900974u>.
- [3] Y.U. Paulechka, Heat Capacity of Room-Temperature Ionic Liquids: A Critical Review., *J. Phys. Chem. Ref. Data*. 39 (2010) 33108–33123. <https://doi.org/10.1063/1.3463478>.
- [4] W. Silva, M. Zanatta, A.S. Ferreira, M.C. Corvo, E.J. Cabrita, Revisiting ionic liquid structure-property relationship: A critical analysis, *Int. J. Mol. Sci.* 21 (2020). <https://doi.org/10.3390/ijms21207745>.
- [5] S. Jiang, Y. Hu, Y. Wang, X. Wang, Viscosity of typical room-temperature ionic liquids: A critical review, *J. Phys. Chem. Ref. Data*. 48 (2019) 33101. <https://doi.org/10.1063/1.5090486>.
- [6] J.M.S.S. Esperança, J.N. Canongia Lopes, M. Tariq, L.M.N.B.. Santos, J.W. Magee, L.P.N. Rebelo, Volatility of aprotic ionic liquids — a review, *J. Chem. Eng. Data*. 55 (2010) 3–12. <https://doi.org/10.1021/je900458w>.
- [7] X. Wang, Y. Chi, T. Mu, A review on the transport properties of ionic liquids, *J. Mol. Liq.* 193 (2014) 262–266. <https://doi.org/10.1016/J.MOLLIQ.2014.03.011>.
- [8] Inamuddin, A.M. Asiri, Nanotechnology-based industrial applications of ionic liquids, Springer Cham, 2020. <https://doi.org/10.1007/978-3-030-44995-7>.
- [9] H. Karkhanechi, S. Salmani, M. Asghari, A review on gas separation applications of supported ionic liquid membranes, *ChemBioEng Rev.* 2 (2015) 290–302. <https://doi.org/https://doi.org/10.1002/cben.201500001>.
- [10] F.J. Hernández Fernández, A. Pérez de los Ríos, J. Quesada-Medina, S. Sánchez-Segado, Ionic liquids as extractor agents and reaction media in ester synthesis, *ChemBioEng Rev.* 2 (2015) 44–53. <https://doi.org/https://doi.org/10.1002/cben.201400019>.
- [11] P. Wolf, M. Aubermann, M. Wolf, T. Bauer, D. Blaumeiser, R. Stepic, C.R. Wick, D.M. Smith, A.-S. Smith, P. Wasserscheid, J. Libuda, M. Haumann, Improving the performance of supported ionic liquid phase (SILP) catalysts for the ultra-low-temperature water–gas shift reaction using metal salt additives, *Green Chem.* 21 (2019) 5008–5018. <https://doi.org/10.1039/C9GC02153A>.
- [12] R. Kukawka, A. Pawlowska-Zygarowicz, J. Dzialkowska, M. Pietrowski, H. Maciejewski, K. Bica, M. Smiglak, Highly effective supported ionic liquid-phase (SILP) catalysts: Characterization and application to the hydrosilylation reaction, *ACS Sustain. Chem. Eng.* 7 (2019) 4699–4706. <https://doi.org/10.1021/acssuschemeng.8b04357>.
- [13] P. McNeice, P.C. Marr, A.C. Marr, Basic ionic liquids for catalysis: the road to greater stability, *Catal. Sci. Technol.* 11 (2021) 726–741. <https://doi.org/10.1039/D0CY02274H>.
- [14] R.L. Vekariya, A review of ionic liquids: Applications towards catalytic organic transformations, *J. Mol. Liq.* 227 (2017) 44–60. <https://doi.org/https://doi.org/10.1016/j.molliq.2016.11.123>.
- [15] H.-P. Steinrück, P. Wasserscheid, Ionic liquids in catalysis, *Catal. Letters*. 145 (2015) 380–397. <https://doi.org/10.1007/s10562-014-1435-x>.
- [16] V.C. Ramos, W. Han, X. Zhang, S. Zhang, K.L. Yeung, Supported ionic liquids for air purification, *Curr. Opin. Green Sustain. Chem.* 25 (2020) 100391. <https://doi.org/10.1016/J.COCS.2020.100391>.
- [17] F. Endres, A. Abbott, D.R. MacFarlane, *Electrodeposition from Ionic Liquids*, John Wiley & Sons, Ltd, 2017. <https://wiley-vch.e-bookshelf.de/products/reading-epub/product-id/9598211>.

- [18] M.B. Shiflett, Commercial applications of Ionic Liquids, Springer Cham, 2020. <https://doi.org/10.1007/978-3-030-35245-5>.
- [19] O. Kuzmina, J. Hallett, Application, purification, and recovery of Ionic Liquids, Elsevier Ltd., 2016. <https://www.elsevier.com/books/application-purification-and-recovery-of-ionic-liquids/kuzmina/978-0-444-63713-0>.
- [20] P. Wasserscheid, T. Welton, Ionic Liquids in Synthesis, 2nd ed., Wiley-VCH Verlag GmbH & Co. KGaA, 2007. <https://doi.org/doi:10.1002/9783527621194>.
- [21] M.T. Clough, K. Geyer, P.A. Hunt, J. Mertes, T. Welton, Thermal decomposition of carboxylate ionic liquids: trends and mechanisms, *Phys. Chem. Chem. Phys.* 15 (2013) 20480–20495. <https://doi.org/10.1039/C3CP53648C>.
- [22] A. Ostonen, J. Bervas, P. Uusi-Kyyny, V. Alopaeus, D.H.D.H. Zaitsau, V.N. Emel'Yanenko, C. Schick, A.W.T.A.W.T. King, J. Helminen, I. Kilpeläinen, A.A.A.A. Khachatryan, M.A.M.A. Varfolomeev, S.P.S.P. Verevkin, Experimental and theoretical thermodynamic study of distillable ionic liquid 1,5-diazabicyclo[4.3.0]non-5-enium acetate, *Ind. Eng. Chem. Res.* 55 (2016) 10445–10454. <https://doi.org/10.1021/acs.iecr.6b02417>.
- [23] A. Parviainen, R. Wahlström, U. Liimatainen, T. Liitiä, S. Rovio, J.K.J. Helminen, U. Hyväkkö, A.W.T. King, A. Suurnäkki, I. Kilpeläinen, Sustainability of cellulose dissolution and regeneration in 1,5-diazabicyclo[4.3.0]non-5-enium acetate: a batch simulation of the IONCELL-F process, *RSC Adv.* 5 (2015) 69728–69737. <https://doi.org/10.1039/C5RA12386K>.
- [24] I.F. Mena, E. Diaz, J. Palomar, J.J. Rodriguez, A.F. Mohedano, Cation and anion effect on the biodegradability and toxicity of imidazolium– and choline–based ionic liquids, *Chemosphere.* 240 (2020) 124947. <https://doi.org/10.1016/J.CHEMOSPHERE.2019.124947>.
- [25] N. Sun, M. Rahman, Y. Qin, M.L. Maxim, H. Rodríguez, R.D. Rogers, Complete dissolution and partial delignification of wood in the ionic liquid 1-ethyl-3-methylimidazolium acetate, *Green Chem.* 11 (2009) 646–655. <https://doi.org/10.1039/B822702K>.
- [26] S. Singh, B.A. Simmons, K.P. Vogel, Visualization of biomass solubilization and cellulose regeneration during ionic liquid pretreatment of switchgrass, *Biotechnol. Bioeng.* 104 (2009) 68–75. <https://doi.org/https://doi.org/10.1002/bit.22386>.
- [27] F. Hermanutz, F. Gähr, E. Uerdingen, F. Meister, B. Kosan, New developments in dissolving and processing of cellulose in Ionic Liquids, *Macromol. Symp.* 262 (2008) 23–27. <https://doi.org/https://doi.org/10.1002/masy.200850203>.
- [28] B. Kosan, C. Michels, F. Meister, Dissolution and forming of cellulose with ionic liquids, *Cellulose.* 15 (2008) 59–66. <https://doi.org/10.1007/s10570-007-9160-x>.
- [29] H. Zhao, C.L. Jones, G.A. Baker, S. Xia, O. Olubajo, V.N. Person, Regenerating cellulose from ionic liquids for an accelerated enzymatic hydrolysis, *J. Biotechnol.* 139 (2009) 47–54. <https://doi.org/10.1016/J.JBIOTECH.2008.08.009>.
- [30] F. Zhang, F. Zheng, X. Wu, X. Yang, Q. Zhang, Y. Yin, Thermophysical properties of [EMIm]Ac and its binary and ternary mixtures with water and graphene nanoplatelets for absorption refrigeration, *AIP Adv.* 9 (2019) 055124. <https://doi.org/10.1063/1.5096012>.
- [31] F. Yan, S. Xia, Q. Wang, P. Ma, Predicting the decomposition temperature of ionic liquids by the quantitative structure-property relationship method using a new topological index, *J. Chem. Eng. Data.* 57 (2012) 805–810. <https://doi.org/10.1021/je201023a>.
- [32] Y. Cao, T. Mu, Comprehensive investigation on the thermal stability of 66 ionic liquids by thermogravimetric analysis, *Ind. Eng. Chem. Res.* 53 (2014) 8651–8664.

<https://doi.org/10.1021/ie5009597>.

- [33] C. Maton, N. De Vos, C. V Stevens, Ionic liquid thermal stabilities: decomposition mechanisms and analysis tools, *Chem. Soc. Rev.* 42 (2013) 5963–5977. <https://doi.org/10.1039/C3CS60071H>.
- [34] W. Al-Sallami, P. Parsaeian, A. Neville, An appraisal of the thermal decomposition mechanisms of ILs as potential lubricants, *Lubr. Sci.* 31 (2019) 229–238. <https://doi.org/10.1002/lis.1457>.
- [35] D.H. Zaitsau, A. Abdelaziz, The study of decomposition of 1-ethyl-3-methyl-imidazolium bis(trifluoromethylsulfonyl)imide by using Termogravimetry: Dissecting vaporization and decomposition of ILs, *J. Mol. Liq.* 313 (2020) 113507. <https://doi.org/https://doi.org/10.1016/j.molliq.2020.113507>.
- [36] J.A. Lazzús, A group contribution method to predict the thermal decomposition temperature of ionic liquids, *J. Mol. Liq.* 168 (2012) 87–93. <https://doi.org/10.1016/j.molliq.2012.01.011>.
- [37] H.T. Do, Y.Z. Chua, J. Habicht, M. Klinksiek, S. Volpert, M. Hallermann, M. Thome, D. Pabsch, D. Zaitsau, C. Schick, C. Held, Melting properties of peptides and their solubility in water. Part 2: di- and tripeptides based on glycine, alanine, leucine, proline, and serine, *Ind. Eng. Chem. Res.* 60 (2021) 4693–4704. <https://doi.org/10.1021/acs.iecr.0c05652>.
- [38] H.T. Do, Y.Z. Chua, A. Kumar, D. Pabsch, M. Hallermann, D. Zaitsau, C. Schick, C. Held, Melting properties of amino acids and their solubility in water, *RSC Adv.* 10 (2020) 44205–44215. <https://doi.org/10.1039/D0RA08947H>.
- [39] H.T. Do, Y.Z. Chua, J. Habicht, M. Klinksiek, M. Hallermann, D. Zaitsau, C. Schick, C. Held, Melting properties of peptides and their solubility in water. Part 1: Dipeptides based on glycine or alanine, *RSC Adv.* 9 (2019). <https://doi.org/10.1039/c9ra05730g>.
- [40] A. Abdelaziz, D.H. Zaitsau, N. V. Kuratieva, S.P. Verevkin, C. Schick, Melting of nucleobases. Getting the cutting edge of “walden’s Rule,” *Phys. Chem. Chem. Phys.* 21 (2019) 12787–12797. <https://doi.org/10.1039/c9cp00716d>.
- [41] Y.Z. Chua, H.T. Do, C. Schick, D. Zaitsau, C. Held, New experimental melting properties as access for predicting amino-acid solubility, *RSC Adv.* 8 (2018) 6365–6372. <https://doi.org/10.1039/c8ra00334c>.
- [42] A. Abdelaziz, D.H. Zaitsau, T.A. Mukhametzyanov, B.N. Solomonov, P. Cebe, S.P. Verevkin, C. Schick, Melting temperature and heat of fusion of cytosine revealed from fast scanning calorimetry, *Thermochim. Acta.* 657 (2017) 47–55. <https://doi.org/10.1016/j.tca.2017.09.013>.
- [43] S. Vyazovkin, A.K. Burnham, J.M. Criado, L.A. Pérez-Maqueda, C. Popescu, N. Sbirrazzuoli, ICTAC Kinetics Committee recommendations for performing kinetic computations on thermal analysis data, *Thermochim. Acta.* 520 (2011) 1–19. <https://doi.org/10.1016/J.TCA.2011.03.034>.
- [44] S. Vyazovkin, *Isoconversional kinetics of thermally stimulated processes*, 2015. <https://doi.org/10.1007/978-3-319-14175-6>.
- [45] J. Šesták, G. Berggren, Study of the kinetics of the mechanism of solid-state reactions at increasing temperatures, *Thermochim. Acta.* 3 (1971) 1–12. [https://doi.org/10.1016/0040-6031\(71\)85051-7](https://doi.org/10.1016/0040-6031(71)85051-7).
- [46] L.A. Pérez-Maqueda, J.M. Criado, P.E. Sánchez-Jiménez, L. A. Pérez-Maqueda, J. M. Criado, P. E. Sánchez-Jiménez, L.A. Pérez-Maqueda, J.M. Criado, P.E. Sánchez-Jiménez, L. A. Pérez-Maqueda, J. M. Criado, P. E. Sánchez-Jiménez, Combined kinetic analysis of solid-state reactions: A powerful tool for the simultaneous determination of kinetic parameters and the

- kinetic model without previous assumptions on the reaction mechanism, *J. Phys. Chem. A.* 110 (2006) 12456–12462. <https://doi.org/10.1021/jp064792g>.
- [47] M.J. Frisch, G.W. Trucks, H.B. Schlegel, G.E. Scuseria, M.A. Robb, J.R. Cheeseman, G. Scalmani, V. Barone, G.A. Petersson, H. Nakatsuji, X. Li, M. Caricato, A. V. Marenich, J. Bloino, B.G. Janesko, R. Gomperts, B. Mennucci, H.P. Hratchian, J. V. Ortiz, A.F. Izmaylov, J.L. Sonnenberg, D. Williams-Young, F. Ding, F. Lipparini, F. Egidi, J. Goings, B. Peng, A. Petrone, T. Henderson, D. Ranasinghe, V.G. Zakrzewski, J. Gao, N. Rega, G. Zheng, W. Liang, M. Hada, M. Ehara, K. Toyota, R. Fukuda, J. Hasegawa, M. Ishida, T. Nakajima, Y. Honda, O. Kitao, H. Nakai, T. Vreven, K. Throssell, J.A. Montgomery Jr., J.E. Peralta, F. Ogliaro, M.J. Bearpark, J.J. Heyd, E.N. Brothers, K.N. Kudin, V.N. Staroverov, T.A. Keith, R. Kobayashi, J. Normand, K. Raghavachari, A.P. Rendell, J.C. Burant, S.S. Iyengar, J. Tomasi, M. Cossi, J.M. Millam, M. Klene, C. Adamo, R. Cammi, J.W. Ochterski, R.L. Martin, K. Morokuma, O. Farkas, J.B. Foresman, D.J. Fox, *Gaussian 16 Revision B.01*, (2016).
- [48] S. Grimme, F. Bohle, A. Hansen, P. Pracht, S. Spicher, M. Stahn, Efficient quantum chemical calculation of structure ensembles and free energies for nonrigid molecules, *American Chemical Society*, 2021. <https://doi.org/10.1021/acs.jpca.1c00971>.
- [49] F. Neese, Software update: the ORCA program system, version 4.0, *Wiley Interdiscip. Rev. Comput. Mol. Sci.* 8 (2018) e1327. <https://doi.org/10.1002/wcms.1327>.
- [50] F. Neese, E.F. Valeev, Revisiting the atomic natural orbital approach for basis sets: Robust systematic basis sets for explicitly correlated and conventional correlated ab initio methods?, *J. Chem. Theory Comput.* 7 (2011) 33–43. <https://doi.org/10.1021/ct100396y>.
- [51] D. G. Liakos, M. Sparta, M. K. Kesharwani, J. M. L. Martin, F. Neese, D.G. Liakos, M. Sparta, M.K. Kesharwani, J.M.L. Martin, F. Neese, Exploring the accuracy limits of local pair natural orbital coupled-cluster theory, *J. Chem. Theory Comput.* 11 (2015) 1525–1539. <https://doi.org/10.1021/ct501129s>.
- [52] A. Ghysels, T. Verstraelen, K. Hemelsoet, M. Waroquier, V. Van Speybroeck, TAMkin: A versatile package for vibrational analysis and chemical kinetics, *J. Chem. Inf. Model.* 50 (2010) 1736–1750. <https://doi.org/10.1021/ci100099g>.
- [53] COSMOtherm, (2020). <http://www.3ds.com>.
- [54] A. Klamt, Conductor-like screening model for real solvents: A new approach to the quantitative calculation of solvation phenomena, *J. Phys. Chem.* 99 (2002) 2224–2235. <https://doi.org/10.1021/j100007a062>.
- [55] A. Klamt, V. Jonas, T. Bürger, J.C.W. Lohrenz, Refinement and parametrization of COSMO-RS, *J. Phys. Chem. A.* 102 (1998) 5074–5085. <https://doi.org/10.1021/jp980017s>.
- [56] F. Eckert, A. Klamt, Fast solvent screening via quantum chemistry: COSMO-RS approach, *AIChE J.* 48 (2002) 369–385. <https://doi.org/10.1002/aic.690480220>.
- [57] S.G. Balasubramani, G.P. Chen, S. Coriani, M. Diedenhofen, M.S. Frank, Y.J. Franzke, F. Furche, R. Grotjahn, M.E. Harding, C. Hättig, A. Hellweg, B. Helmich-Paris, C. Holzer, U. Huniar, M. Kaupp, A. Marefat Khah, S. Karbalaei Khani, T. Müller, F. Mack, B.D. Nguyen, S.M. Parker, E. Perlt, D. Rappoport, K. Reiter, S. Roy, M. Rückert, G. Schmitz, M. Sierka, E. Tapavicza, D.P. Tew, C. van Wüllen, V.K. Voora, F. Weigend, A. Wodyński, J.M. Yu, TURBOMOLE: Modular program suite for ab initio quantum-chemical and condensed-matter simulations, *J. Chem. Phys.* 152 (2020) 184107. <https://doi.org/10.1063/5.0004635>.
- [58] L.C. Kröger, W.A. Kopp, K. Leonhard, Prediction of chain propagation rate constants of polymerization reactions in aqueous NIPAM/BIS and VCL/BIS systems, *J. Phys. Chem. B.* 121 (2017) 2887–2895. <https://doi.org/10.1021/acs.jpcc.6b09147>.

- [59] W.A. Kopp, M.L. Mödden, N. Viswanathan, G. Rath, K. Leonhard, Improved modeling of anharmonicity for furan microsolvation, *Phys. Chem. Chem. Phys.* 25 (2023) 11316–11323. <https://doi.org/10.1039/D2CP03907A>.
- [60] C. Gertig, L. Fleitmann, J. Schilling, K. Leonhard, A. Bardow, Rx-COSMO-CAMPD: Enhancing reactions by integrated computer-aided design of solvents and processes based on quantum chemistry, *Chemie-Ingenieur-Technik*. 92 (2020) 1489–1500. <https://doi.org/10.1002/cite.202000112>.
- [61] J.R. Pliego, J.M. Riveros, The cluster–continuum model for the calculation of the solvation free energy of ionic species, *J. Phys. Chem. A*. 105 (2001) 7241–7247. <https://doi.org/10.1021/jp004192w>.
- [62] M.L. Williams, J.S. Dickmann, M.E. McCorkill, J.C. Hassler, E. Kiran, The kinetics of thermal decomposition of 1-alkyl-3-methylimidazolium chloride ionic liquids under isothermal and non-isothermal conditions, *Thermochim. Acta*. 685 (2020) 178509. <https://doi.org/10.1016/J.TCA.2020.178509>.
- [63] C.Y. Legault, CYLview20, (2020). <http://www.cylview.org>.
- [64] M. Królikowska, N. Gos, M. Skonieczny, Temperature and composition dependence of the thermodynamic properties of an aqueous solution of 1-ethyl-3-methylimidazolium formate and 1-ethyl-3-methylimidazolium acetate, *J. Chem. Eng. Data*. 66 (2021) 3300–3314. <https://doi.org/10.1021/acs.jced.1c00349>.